# Design, Fabrication, and Performance of Infrared and Visible Vertical-Cavity Surface-Emitting Lasers

Weng W. Chow, Kent D. Choquette, Mary H. Crawford, Kevin L. Lear, *Member, IEEE,* and G. Ronald Hadley, *Senior Member, IEEE*

*(Invited Paper)*

***Abstract*— This paper discusses the issues involving the design and fabrication of vertical-cavity surface-emitting lasers (VCSEL's). A review of the basic experimental structures is given, with emphasis on recent developments in distributed Bragg reflectors, gain media, as well as current and optical confinement techniques. The paper describes present VCSEL performance, in particular, those involving selective oxidation and visible wavelength operation.**

***Index Terms*— Optoelectronic devices, semiconductor device fabrication, semiconductor lasers.**

## I. Introduction

IN THE 1970's, Iga *et al.* at the Tokyo Institute of Technology, Tokyo, Japan, proposed the idea of a vertical-cavity surface-emitting laser (VCSEL) [1]. They achieved room-temperature pulsed operation in 1984 [2], and continuous-wave (CW) room-temperature operation in 1988 [3]. Since the mid-1980's, the state-of-the-art has progressed steadily, due to advances in the design and growth of mirrors and gain structures, as well as fabrication techniques for electrical and optical confinement. These advances have led to VCSEL's which rival conventional edge-emitting laser diodes in efficiency [4], [5] and surpass them by a wide margin in threshold current [6]–[8]. Several companies are presently manufacturing VCSEL's, and the use of VCSEL's in commercial products is imminent.

The reason many laboratories devote their resources to developing VCSEL technology is because of the concept's inherent advantages. To appreciate these advantages, let us first mention a few problems with conventional diode lasers. The conventional laser is often referred to as an edge emitter because laser output is from the edge of a semiconductor chip [see Fig. 1(a)]. With edge emission, the transverse and lateral modes of the laser depend on the cross section of the heterostructure gain region, which is transversely very thin for carrier confinement and laterally wide for output power. The result is highly elongated near and far fields that do not match well to the circular cross section of an optical fiber. Also, the output beam is highly astigmatic, with full angle beam divergence of as much as 50° in the transverse dimension. This makes the design and fabrication of coupling optics challenging. From a manufacturing aspect, facet mirrors are fabricated either by cleaving or etching, so that optical testing of the laser chip cannot be performed until many of the fabrication and packaging processes are completed. Lastly, due to the long ($10^2$ to $10^3\lambda$) optical cavity, an edge emitter typically lases on multiple longitudinal modes, or is prone to mode hop. While each of the above problems can be addressed at least in part by special structures, these structures add to the complexity and cost of the laser diodes.

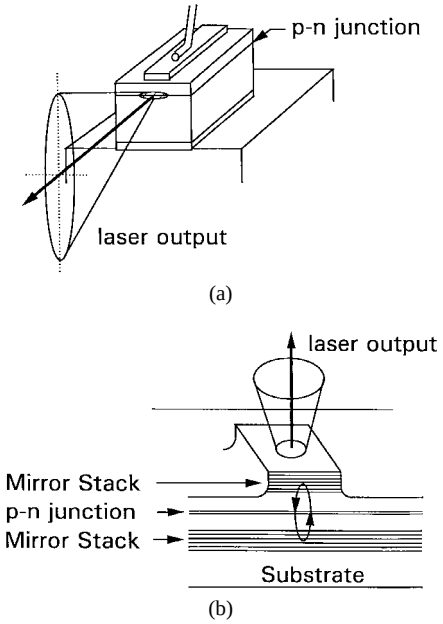


Fig. 1. Schematic drawing of (a) an edge-emitting laser and (b) a VCSEL.

The VCSEL circumvents the problems arising from edge emission by having its resonator axis in the vertical (epitaxial growth) direction [see Fig. 1(b)]. With the laser emission from the wafer surface, it is possible to have a symmetrical beam cross section, with small beam divergence. Furthermore, the very short cavity length makes VCSEL operation inherently single longitudinal mode. Surface emission also make possible the fabrication of two-dimensional (2-D) laser arrays with high fill factors. In addition, there are advantages associated with

Manuscript received January 7, 1997; revised June 10, 1997. This work was supported by the U.S. Department of Energy under Contract DE-AC04-94AL85000.

W. W. Chow, K. D. Choquette, M. H. Crawford, and G. R. Hadley are with Sandia National Laboratories, Albuquerque, NM 87185-0601 USA.

K. L. Lear was with Sandia National Laboratories, Albuquerque, NM 87185-0601 USA. He is now with Micro Optical Devices, Inc., Albuquerque, NM 87109 USA.

Publisher Item Identifier S 0018-9197(97)07074-7.

growth and fabrication. Unlike an edge emitter, the VCSEL mirrors are fabricated during the epitxial growth, thereby eliminating the labor-intensive cleaving or dry etching steps used in making edge-emitting resonator facets. The ability to perform batch processing with standard integrated circuit fabrication technologies, coupled with on-wafer device testing, should enable high-volume and low-cost VCSEL manufacturing.

The advantages of VCSEL's come with a price. The significant reduction in the gain length has to be compensated by a high-$Q$ cavity, which places considerable demand on resonator mirror quality. In Section II, the development of distributed Bragg reflectors (DBR's) as VCSEL resonator mirrors is described. We will emphasize semiconductor mirrors, which enable monolithic VCSEL structures, and allow current injection through the mirrors. The latter requires low electrical resistance in the mirrors, and Section II presents in detail how this can be accomplished with graded DBR structures. Presently, laser performance achievable with conducting mirrors surpasses that of VCSEL configurations where the current paths bypass the mirrors.

The short gain length must also be compensated by an active medium that is capable of providing significant gain to the lasing mode. In Section III, the active region is discussed, in particular, the role it plays in determining threshold properties. We introduce a microscopic gain model and show how it is used to analyze experimental data, such as those relating to spectral and device size dependences. Also in this section is a discussion of the techniques and issues concerning the fabrication of visible wavelength VCSEL's, which presently operate CW from 690 to 630 nm.

Section IV reviews the VCSEL structures used for transverse optical and electrical confinement, which is necessary for achieving high efficiency or low threshold current. Fig. 2 shows the four basic device structures: the etched air-post, ion implanted, regrown buried heterostructure, and oxide-confined VCSEL structures. These devices involve a variety of fabrication techniques. Early VCSEL's used etched air-post structures to confine the current path and to provide index guiding for the optical mode. In contrast, VCSEL's that are created by ion implant have current paths that are defined by the surrounding high-resistance regions. Implanted VCSEL's do not have built-in index guiding for the optical mode. Regrowth allows the fabrication of buried heterostructures, which provide both carrier confinement and index guiding. Recently, oxide-confined structures are found to be highly effective in providing electrical and optical confinement. These structures make possible the demonstration of the highest wall plug efficiency for a VCSEL and the lowest threshold current for a semiconductor laser.

Section V presents a summary of this paper and discusses future research directions and emerging applications.

## II. Distributed Bragg Reflectors (DBR's)

As shown in Fig. 1(b), two DBR's provide longitudinal confinement of the laser field. A typical DBR has several periods, where each period contains a high refractive index layer adjacent to a low refractive index layer. For constructive

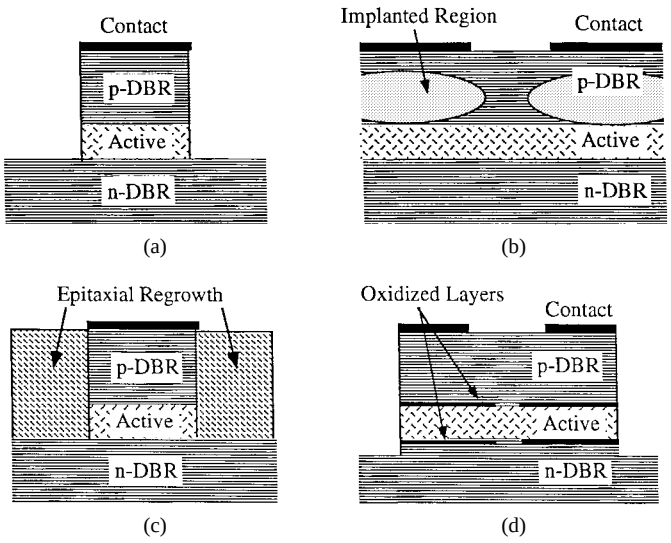


Fig. 2. Four basic structures: (a) etched air-post, (b) ion-implanted, (c) regrown buried heterostructure, and (d) oxide-confined VCSEL's.

interference of the reflected waves from the interfaces, each layer should be $\lambda/4$ thick, where $\lambda$ is the wavelength in the respective layers. The choice of materials for the layers is based on maximizing index contrast, and maintaining transparency to the laser light. The layers may be made of dielectric materials, where a large refractive index difference between layers is possible (e.g., $n(\mathrm{ZnSe}) - n(\mathrm{CaF_2}) = 1.7$) [9], so that one obtains high reflectivity with a small number of DBR periods. We, as well as others, have concentrated on the development of semiconductor DBR's [10], [11], because they can be epitaxially grown and allow current injection through the mirrors. However, the index contrast ($\mathrm{n(GaAs)} - \mathrm{n(AlAs)} = 1.2$) is not as high as in a dielectric DBR, and consequently, a large number ($>20$) of periods is needed to achieve high reflectivity. The combinations of $\mathrm{Al_{0.2}Ga_{0.8}As}$–AlAs and GaAs–AlAs are typical for VCSEL's operating at 850 and 980 nm, respectively. In a semiconductor system that lacks sufficiently high index contrast alloys, a solution is to grow nonlattice-matched DBR's, and then wafer bond them to the optical cavity. For example, DBR mirrors consisting of GaAs–AlAs layers have been grown separately and then wafer bonded to phosphide-based alloys for operation at 1.3 and 1.55 $\mu$m [12].

An important issue associated with current injection through a DBR is electrical resistance. Heterojunctions between high- and low-index semiconductors usually have large energy band offsets that form potential barriers which inhibit carrier flow. This problem can be particularly acute in p-type DBR's because the large hole mass reduces tunneling and thermionic emission. While the heterojunction resistance can be reduced by increased doping, one cannot arbitrarily increase doping densities throughout the structure, because doing so also increases optical absorption. A more effective solution is the use of alloy grading at interfaces, often in conjunction with varied doping profiles such as increased doping at interfaces [13], delta doping [14], and modulation doping [15]. Initial demonstrations of interface grading used a single narrow region of intermediate alloy composition inserted between the

high- and low-index layers [16]. Such step grading profiles substantially reduce the differential resistance at large electrical biases, but typically result in DBR voltage drops of 1 V or more even at modest current densities of 1 kA·cm$^{-2}$.

Further reductions in DBR voltage result from more continuous variations in alloy composition across the interface. In conventional molecular beam epitaxy (MBE), the alloy composition changes discontinuously between values determined by the fixed fluxes of a limited number of Al and Ga effusion cells. Alternatively, superlattices with effective intermediate compositions can be created by alternating thin layers of just two compositions. The latter technique provides the ability to vary the effective alloy composition using a minimum number of cells simply by varying the duty cycle of the superlattice. Superlattice grading has the disadvantage of requiring thousands of shutter operations per VCSEL growth. True alloy grading can also be achieved by MBE through variation of the cell temperatures [17].

The cell temperature variation technique was used to realize two of the grading configurations shown in Fig. 3(a) [18]. The DBR composition was ramped continuously from $Al_{0.1}Ga_{0.9}As$ to $Al_{0.9}Ga_{0.1}As$ and back again to $Al_{0.1}Ga_{0.9}As$ by cyclically varying the Al and Ga effusion cell temperatures in complementary fashion. In the first case, shown by the dashed line in Fig. 3(a), the alloy composition is varied linearly between the two extreme compositions. More complicated profiles are also possible as illustrated with the dotted line which uses three piecewise linear segments at each interface. The latter profile reduces the potential cusps which form at grading rate discontinuities [18] and thus yields lower voltage drops than the simple linear grading as seen in Fig. 3(b). Note that the current–voltage relationship is linear for the three-segment-per-interface profile, indicating a substantial elimination of potential barriers that cause nonlinear transport due to tunneling and thermionic emission.

In addition to the resistance of DBR's to vertical current flow, other properties including electrical lateral resistance, thermal resistance, and optical reflectivity must be considered in the design of DBR grading. While the vertical electrical resistance is lowest for long graded regions and reduced alloy composition variation, the other properties benefit from reduced alloy content. Thus the alloy grading should be concentrated at the approach to the high bandgap material where it has the most benefit for reducing the vertical electrical resistance. This consideration motivates the grading profile shown by the solid line in Fig. 3(a) [19]. It has lower alloy content in the flat regions as well as a more narrow transition region in between. Despite the reduced alloy content, Fig. 3(b) shows that this last design implemented with metalorganic vapor phase epitaxy (MOVPE) has the lowest voltage drop of the three DBR's. While this profile could have been realized with MBE using the cell temperature variation technique, it is more simply realized using MOVPE [20]. Another advantage that MOVPE offers over conventional MBE is the use of carbon as a p-type dopant which has lower diffusivity and is more readily activated in AlAs than Be.

Other significant contributions to the voltage drop in VCSEL's are the lateral spreading and contact resistances. Both

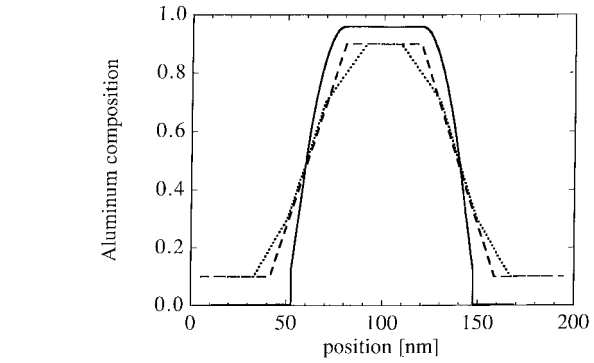


(a)

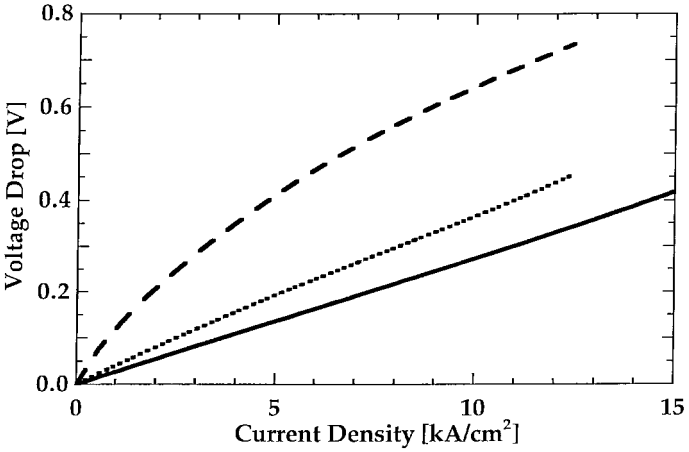


(b)

Fig. 3. (a) Three different grading profiles used in 20-period DBR's and (b) the resulting voltage–current density relationships. The grading profiles are linear (dashed), three linear segments per interface (dotted), and uniparabolic (solid). The average dopant concentrations are $2.9 \times 10^{18}$ (Be), $1.9 \times 10^{18}$ (Be), and $2.0 \times 10^{18}$ (C), respectively. The first two were grown by MBE and the third was grown by MOVPE.

contributions are accentuated in laterally contacted geometries, such as those used in top emitting devices. The points in Fig. 4 show the measured device resistance for VCSEL's with cross-sectional areas defined by proton implantation [see Fig. 2(b)]. The two groups of points correspond to the three-segment-per-interface and uniparabolic designs shown in Fig. 3. Each group may be fitted with the expression [21]

$$R = \frac{R_L}{2\pi r} + \frac{R_V}{\pi r^2} \tag{1}$$

where the first term accounts for the contact, lateral, and constriction contributions, and the second term accounts for the heterojunction resistance. The curves in the figure are fits to experimental data, using (1). The fitting parameters are $R_L$ =4.1 and 1.0 Ω·mm and $R_V = 2.6\times10^{-5}$ and $9.8\times10^{-6}$ Ω·cm$^2$ for the upper and lower curves, respectively. For both curves, the first term dominates for device radii, $r > 1$ $\mu$m, emphasizing the importance of reducing lateral and contact resistance in top-emitting VCSEL's. This is accomplished in part by the inclusion of an extra $\lambda/2$ layer of heavily doped GaAs at the surface of the MOVPE lasers with the uniparabolic mirror [19].

Fabrication also influences the lateral resistance of annular-contacted VCSEL structures. Damage caused by proton implantation increases both bulk and contact resistivity. To

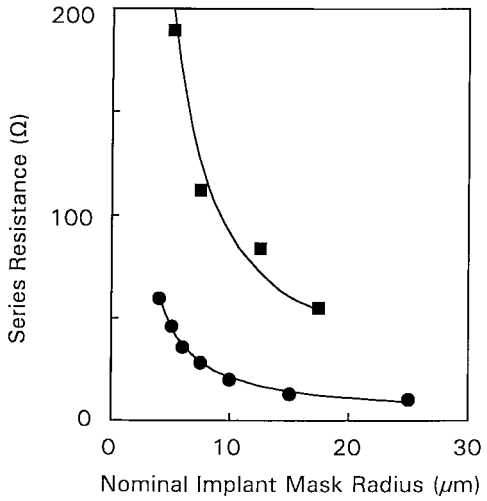


Fig. 4. Series resistance versus active region radius for proton implanted VCSEL's with two DBR designs described in the text.

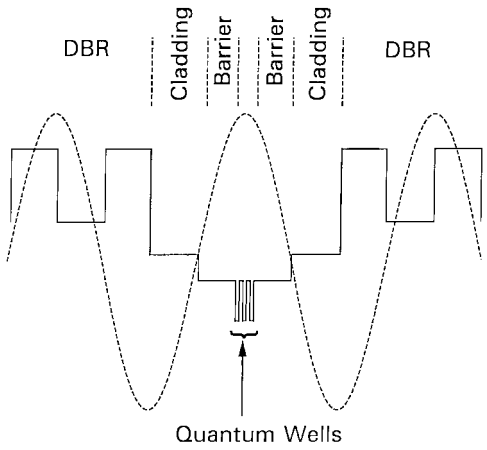


Fig. 5. Conduction band edge energy as a function of position along the laser axis, for a general QW VCSEL structure. The dashed curve shows the optical mode longitudinal spatial profile for a $1\lambda$ cavity.

minimize detrimental effects of the implant, the implant dose is made as low as possible. Excessive damage can be partially annealed in a furnace or through operation of the laser [22]. The sensitivity of contact resistance to implant damage can be reduced by increasing the doping level near the surface, for example, by using beryllium delta doping in conjunction with thin InGaAs caps [21]. Carbon doping also permits high $(p > 5 \times 10^{19})$ cap doping in MOVPE material.

## III. Active Region

### A. Gain Structure

With high-reflectivity DBR's, material threshold gain in a VCSEL lies in the range between hundreds to thousands of inverse centimeters. For a current injection device, the gain typically comes from a quantum-well (QW) structure. Fig. 5 shows the conduction band edge energy as a function of position along the laser axis, for a general QW VCSEL structure. The valence band edge energy is similar except for the magnitude of the band offsets. The extent of the optical cavity is defined by the DBR's. Inside the optical cavity is the QW active region. In the case of multiple QW's, they are separated by barrier layers. Cladding layers make up the remainder of the usually $1\lambda$-thick optical cavity.

The dashed curve in Fig. 5 shows the field amplitude of the lasing mode for a $1\lambda$ cavity. The placement of the QW's in relation to the lasing mode is important because it determines the longitudinal confinement factor. The confinement factor measures the overlap between the gain region and the lasing mode, and is one of the factors determining the effectiveness of the active region in providing gain to the lasing mode. Compared to a spatially uniform gain distribution, a factor-of-two enhancement in the longitudinal confinement factor results if the active region is concentrated at the antinodes of the lasing mode [23]. In the case of a $1\lambda$ cavity, which has only one antinode centered within the optical cavity, space constraint limits the number of QW's that can be packed around the antinode. The optimal number balances the increase in gain length and the reduction in confinement factor with increasing number of QW's.

A wide range of III–V compounds are used in VCSEL active regions. An extensively studied active region consists of InGaAs QW's separated by GaAs barrier layers. The ability to change the amount of compressive strain in a QW by changing the In concentration makes accessible a lasing wavelength range of 0.9–1 $\mu$m. This wavelength range also has the practical advantage of the GaAs substrate being transparent to the laser output. Compressive strain increases the curvature of the lowest energy hole band, which increases the gain for a given carrier density. The high gain and low absorption losses achievable with an InGaAs QW gain region make possible the demonstration of many VCSEL concepts, such as those leading to ultralow threshold current, or very high efficiency VCSEL's. Other gain regions are GaAs–AlGaAs QW structures for operation in the 780–870-nm wavelength range, InGaAsP–InP for the longer wavelengths around 1.3–1.6 $\mu$m, and InGaP–InAlGaP for the visible region from approximately 630 to 690 nm.

Because of quantum confinement, strain, and the wide range of active region materials, we have the potential to tailor a gain structure to optimize desired laser properties. In order to realize this potential, an understanding of active medium properties and dependences is important. An expeditious way to expand our knowledge base and gain an understanding of the underlying physics governing active region behavior is with a microscopic gain model, where the influences of the band structure, as well as the dependences on wavelength and carrier density, are described [24]–[26].

### B. Gain Model

In this subsection, we describe a gain model that has been particularly successful at predicting the carrier density and band structure dependences of the gain spectrum [27]–[29]. This model is based on semiclassical laser theory [30], where one treats the laser field classically and the active medium quantum mechanically. To derive the active medium equations, we use a Hamiltonian that contains the dipole interaction

between the laser field and an electron-hole pair, as well as the Coulomb interactions among carriers. Including the many-body Coulomb interactions is important in order to accurately describe the VCSEL threshold behavior [31]–[33]. Working in the Heisenberg Picture, we derive equations of motion for the active medium polarization and carrier populations (Semiconductor Bloch Equations) [34]. Using the rate-equation approximation, and treating the interband Coulomb interactions as a perturbation, gives the following equation for intensity gain [26], (MKS):

$$G = \frac{\omega}{\epsilon_0 n c \hbar \gamma V} \sum_{\vec{k}} |\mu_{\vec{k}}|^2 (n_{e,\vec{k}} + n_{h,\vec{k}} - 1) L(\omega - \omega_{\vec{k}}) \mathrm{Re}(Q_{\vec{k}}) \tag{2}$$

where $\omega_{\vec{k}}$ is the transition frequency, $\omega$ is the laser frequency, $\epsilon_0$ and $c$ are the permittivity and speed of light in vacuum, $n$ is the background refractive index, $V$ is the active region volume, and $\mu_{\vec{k}}$ is the optical transition dipole matrix element. The lineshape function is usually assumed to be a Lorentzian, $L(x) = [1+(x/\gamma)^2]^{-1}$, or a hyperbolic sech function, $L(x) = \mathrm{sech}(x/\gamma)$, where the dephasing rate, $\gamma$, is an input parameter. The gain is evaluated for quasi-equilibrium conditions, where intraband relaxation is sufficiently fast for the electron and hole distributions, $n_{e,\vec{k}}$ and $n_{h,\vec{k}}$, to be given by Fermi–Dirac functions. The transition frequency and the dipole matrix element depend on the QW band structure. We compute these quantities by using $\vec{k} \cdot \vec{p}$ theory [35], where modifications due to quantum confinement and strain are treated in the context of the envelope approximation [24]. The effects of many-body Coulomb interactions enter into (2) in the form of a carrier density dependence in the transition energy

$$\hbar\omega_{\vec{k}}(N) = \epsilon_{e,\vec{k}} + \epsilon_{h,\vec{k}} + [\epsilon_{g,0} + \Delta\epsilon_{\mathrm{CH}}(N) + \Delta\epsilon_{\mathrm{SX}}(N)] \tag{3}$$

where $\epsilon_{g,0}$ is the unexcited semiconductor bandgap energy, $\Delta_{\mathrm{CH}}$ and $\Delta_{\mathrm{SX}}$ are the Coulomb-hole and screened exchange contributions, respectively, to the renormalized band gap energy. Coulomb effects also result in an excitonic or Coulomb enhancement factor

$$Q_{\vec{k}} = \mu_{\vec{k}} \left[ \mu_{\vec{k}} - \sum_{\vec{k}'} V_{s,|\vec{k}-\vec{k}'|} \frac{n_{e,\vec{k}'} + n_{h,\vec{k}'} - 1}{i\hbar\gamma - \hbar(\omega_{\vec{k}'} - \omega)} \right]^{-1} \tag{4}$$

where $V_{s,q}$ is the Fourier transform of the screened Coulomb potential energy.

### C. Gain Effects on Threshold

We now show how the microscopic gain model can help explain threshold behavior in a VCSEL. VCSEL threshold behavior is strongly affected by the very short ($\approx\lambda$), high-$Q$ optical resonator, whose optical modes are well defined and widely spaced in frequency. As a result, there is often only one longitudinal mode within the gain spectrum, which leads to laser threshold properties that are sensitive to the alignment of the lasing mode in relation to the gain peak [36].

The threshold current and voltage are two important device properties because they affect above-threshold performance as well as electrical requirements for operating the laser. The intrinsic voltage is the lowest achievable potential drop for a device. We can extract this quantity from a voltage versus current (*V–I*) curve [33]. For a *V–I* curve that is linear above threshold, we can determine a series resistance, $R_s$. At lasing threshold, the voltage due to ohmic losses is $I_{\mathrm{th}}R_s$, where $I_{\mathrm{th}}$ is the threshold current. We subtract $I_{\mathrm{th}}R_s$ from the total threshold voltage to get the intrinsic threshold voltage. The points in Fig. 6 show the measured intrinsic voltage for selectively oxidized near-IR VCSEL's distributed across the same wafer. There is sufficient variation in layer thicknesses across the wafer to provide VCSEL's with a range of lasing wavelength. The variation in the intrinsic voltage with lasing wavelength shows the effect of the alignment between the lasing mode and the gain spectrum. The minimum intrinsic voltage is achieved at a wavelength that equals the peak gain wavelength. The increase in voltage with deviation from this wavelength depends on the shape and carrier density dependence of the gain spectrum.

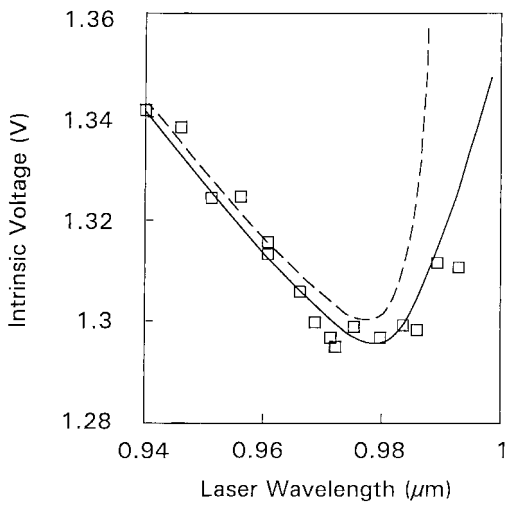


Fig. 6. Intrinsic threshold voltage versus lasing wavelength, from experiment (points), many-body model (solid curve), and free-carrier model (dashed curve).

We assume that the intrinsic device voltage and the energy separation between the electron and hole quasi-equilibrium chemical potentials are equivalent. Since the quasi-equilibrium chemical potential separation depends on the electron and hole densities and the renormalized band gap energy, its changes also result in changes in the magnitude and energy extension of the gain spectrum. The solid curve is the quasi-equilibrium chemical potential separation obtained from (2). For the band structure calculations, we use material parameters reported in the literature [37], [38]. The gain calculations are performed by assuming a sech lineshape function with a dephasing rate of $\gamma = 2\times10^{13}$ s$^{-1}$. Based on the best fit to the experimental data, the theory predicts the same threshold gain of $G_{\mathrm{th}} = 500$ cm$^{-1}$ for all the VCSEL's. The prediction of equal threshold gains is consistent with the VSCEL's being from a small region of the same wafer, where we expect negligible differences in optical and electrical properties, except for the cavity optical path lengths. Note that the gain model is able to describe the voltage behavior for all the devices reasonably well without changing input parameters (except the lasing wavelength). Fig.

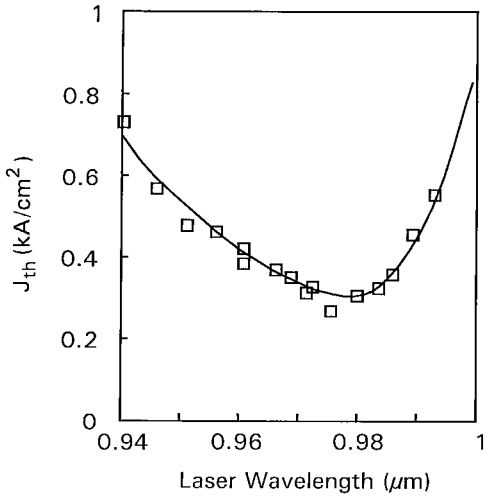


Fig. 7. Threshold current density versus lasing wavelength, from experiment (points), many-body model (solid curve), and free-carrier model (dashed curve).

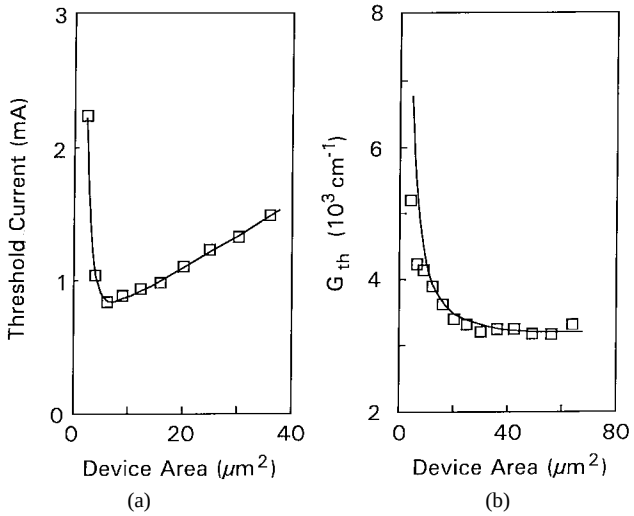


Fig. 8. (a) Measured threshold current vs. emitting cross section area foroxide confined VCSEL. (b) Threshold gain extracted from intrinsic voltage(points) and from physical optics model (curve).

6 also shows the results of neglecting the many-body Coulomb effects (dashed curve). For the shorter wavelength devices, both gain models give basically the same results. However, for the longer wavelength devices, the free-carrier theory predicts significantly higher intrinsic voltages.

Fig. 7 shows the threshold current density for the same devices. The theoretical curve is obtained using the same input parameters as in the intrinsic voltage calculations. In addition to (2), the calculation requires the steady-state solution to the carrier density rate equation

$$J_{\rm th} = eL_g\left[w_{\rm spont}(N_{\rm th}) + \gamma_{\rm nr}N_{\rm th} + CN_{\rm th}^3\right] \tag{5}$$

where $J_{\rm th}$ is the threshold current density, $e$ is the electron charge, $w_{\rm spont}$ is the spontaneous emission contribution computed along with the gain calculations, $N_{\rm th}$ is the threshold carrier density, $\gamma_{\rm nr}$ accounts for nonradiative carrier losses, and $C$ is the Auger coefficient. We account for carrier leakage by including in the analysis the unconfined states of the QW structure and then assuming thermal equilibrium between the populations of these states and the bound QW states [39]. The solid curve, which assumes $G_{\rm th} = 500$ cm$^{-1}$, shows good agreement between theory and experiment.

According to (2) and (5), neither the gain nor the threshold current contain any explicit dependence on the active region cross section. This observation leads to the argument that if one can decrease the active region area and maintain the same threshold current density, then the threshold current will be reduced accordingly. Fig. 8(a) shows this to be the case only for oxide-confined VCSEL's with cross-section areas $>20$ $\mu$m$^2$. To gain an understanding of the VCSEL threshold dependence on device size, we perform the following analysis of the experimental data [40]. Using the microscopic gain model, we extract from the voltage data the threshold gain as a function of device size [points, Fig. 8(b)]. Then, from a physical optics simulation of the VCSEL cavity, we obtain an independent assessment of the threshold gain dependence on device cross section ([curve, Fig. 8(b)]. This latter calculation represents a numerical solution of the scalar Helmholtz equation describing the cavity modes for the actual device geometry. According to various optical models [40], [41], the oxide apertures, which define the gain region cross section, give rise to significant optical losses in the small devices. The calculated scattering and diffraction losses, together with the condition for lasing threshold give the threshold gain

$$G_{\rm th} = \frac{1}{2\Gamma L_g}\left[-\ln(R_1R_2) + l_{\rm ab} + l_{\rm sc}\right] \tag{6}$$

where $R_1$ and $R_2$ are the DBR reflectivities, $\Gamma$ is the confinement factor, and $l_{\rm ab(sc)}$ accounts for the round-trip absorption (scattering) losses. We choose $l_{\rm ab}$ so that both curve and points coincide for the large devices, where scattering losses are negligible. The good agreement between the two results for the entire range of device sizes indicates that the increase in threshold gain with decreasing device cross section is due primarily to diffraction losses from the oxide apertures.

From the threshold gain increase, we can calculate the corresponding increase in the threshold carrier density. Any increase in carrier density inevitably leads to greater leakage of carriers from the QW's. We account for carrier leakage by including in the analysis the unconfined states of the QW structure, and then assuming thermal equilibrium between the populations of these states and the bounded QW states [39]. The solid curve in Fig. 9 shows the calculated results, which agree well with experiment (points). The dashed curve indicates significant contribution from the leakage current for the small devices.

### *D. Toward Visible Wavelengths*

Over the past several years, we have also seen numerous advances in the design and performance of VCSEL's emitting in the visible region of the spectrum [42]. These devices are of interest due to the many visible wavelength applications that can benefit from the geometry and performance of a VCSEL. They include applications where a low divergence beam leads to less expensive optical components, e.g., in

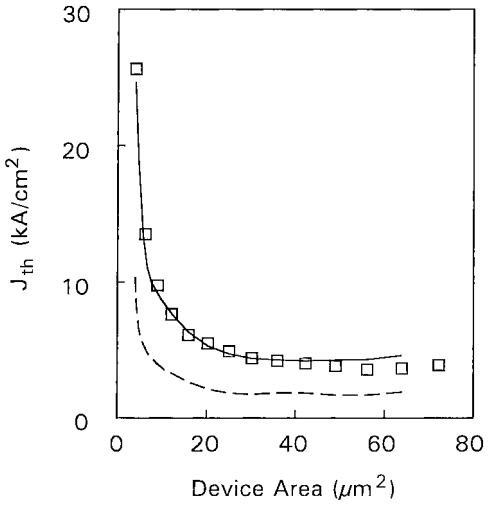


Fig. 9. Threshold current density versus emitting cross-section area from experiment (points) and model (solid curve). The dashed curve shows the calculated leakage current.

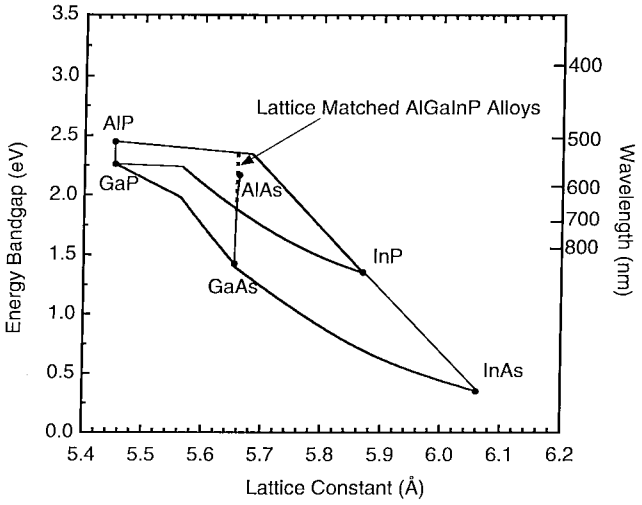


Fig. 10. Room-temperature band-gap energy versus lattice mismatch for alloys of AlGaInP on GaAs substrates.

laser scanners and printers. Visible wavelength VCSEL's are also attractive for plastic fiber-based applications, due to the minimum in the attenuation of the fibers at 650 nm, and to the compatibility of the VCSEL symmetrical beam profile to optical fiber coupling. Finally, there are numerous spectroscopic and medical applications that require low-power compact visible laser sources in the few milliwatt regime.

While VCSEL's emitting in the far visible (700–800 nm) region have been demonstrated using AlGaAs alloys [43], [44], the most efficient visible wavelength VCSEL's to date are composed of AlGaInP alloys. The first electrically injected AlGaInP VCSEL's were demonstrated in 1993 [45]–[47]. Later, the development of a $1\lambda$ cavity design led to rapid progress, resulting in visible VCSEL's with outputs of several milliwatts, and wallplug efficiencies above 10% [48]. Single-mode performance is important for many applications, such as bar-code scanning and spectroscopy. To date, the highest single-mode power achieved is approximately 2 mW at 690 nm, with up to 1-mW single-mode power demonstrated in the 665–675-nm region [49].

Fig. 10 shows that AlGaInP alloys have direct bandgap energies that span the visible region of the spectrum, from deep-red to green. When lattice-matched to GaAs, the QW's may be under tensile and compressive strain, depending on In concentration. The unstrained configuration occurs at an In concentration of 0.52. The quaternary alloy $(Al_xGa_{1-x})_{0.48}In_{0.52}P$ has a $\Gamma - X$ conduction band crossing at an Al mole fraction of approximately 0.56 to 0.7 [50]. This results in a transition from a direct to an indirect bandgap material at approximately 555–570 nm, which is in the green to yellow region of the spectrum. The $\Gamma - X$ crossover limits short-wavelength operation, as well as the bandgap energy available for barrier and cladding materials.

The heterostructure design of AlGaInP VCSEL active regions is more challenging than for AlGaAs based near-infrared (IR) VCSEL's, due to less favorable materials properties. Table I compares some of the relevant material properties for the visible and near-IR wavelength gain structures. The

TABLE I
COMPARISON OF MATERIAL PROPERTIES FOR InGaAsP–AlGaInP AND InGaAs–AlGaAs HETEROSTRUCTURES

| | $In_xGa_{1-x}As$–$Al_{0.4}Ga_{0.6}As$ near-IR | $In_xGa_{1-x}P$–$(Al_{0.5}Ga_{0.5})_{0.5}In_{0.5}P$ visible |
|---|---|---|
| $\Delta E_c$ | 350 meV @ $x = 0$ (L)<br>480 meV @ $x = 0.2$ (S) | 165 meV @ 165 meV (L)<br>225 meV @ $x = 0.6$ (S) |
| $\Delta E_v$ | 220 meV @ $x = 0$ (L)<br>290 meV @ $x = 0.2$ (S) | 110 meV @ $x = 0.5$<br>150 meV @ $x = 0.6$ (S) |
| $m_c^*$ | $0.067m_0$ $(x = 0)$ | $0.11m_0$ $(x = 0.5)$ |
| $m_{hh}^*$ | $0.45m_0$ $(x = 0)$ | $0.62m_0$ $(x = 0.5)$ |
| $W$ | $2 < W < 10$ cm ° C/W | $W \geq 19$ cm ° C/W |

smaller confinement potentials for the former, shown in Table I for both lattice-matched (L) and strained (S) quantum-well structures, means that carrier leakage will be greater. Also, the larger effective masses (relative to the free-electron mass, $m_0$, contribute to higher threshold currents, and the larger thermal impedance $(W)$ leads to greater sensitivity to heating. There are also issues involving doping and atomic ordering [42].

A task that is made more difficult by the shorter wavelength is the design and fabrication of DBR's. At present, the active regions providing gain in the visible portion of the spectrum are based on AlGaInP alloys, while the DBR's typically consist of AlAs–$Al_xGa_{1-x}As$ layers. However, the low-index $Al_xGa_{1-x}As$ layers must have higher Al concentration ($\geq$0.5) to maintain low absorption of the laser light for $\lambda \leq 650$ nm. The higher Al concentration reduces the refractive index contrast ratio, and consequently, a larger number of DBR periods is needed. With $x = 0.5$, the index contrast is $\Delta n/n =$ 11% at 670 nm, and approximately 34 DBR periods are needed to achieve >99.9% reflectivity. With thicker mirrors, series resistance becomes more of a problem. To mitigate the effects of the thicker mirrors, we typically use a parabolically graded transition region between the constituent DBR layers.

For wavelengths shorter than 640 nm, other mirror designs have to be considered. For example, AlInP–AlGaInP layers can be designed for operating from green to red wavelengths [51]. Unfortunately, the index contrast is relatively low, and the electrical resistance is somewhat high. The use of

oxidization lowers the refractive index without increasing absorption. Only five periods of $Al_2O_3/Al_{0.9}Ga_{0.1}As$ are needed to achieve greater than 99.9% reflectivity in the visible. A drawback is that the mirror is not conductive and therefore an intracavity electrical contact is necessary. Similar results have been achieved with AlInP–$Al_2O_3$ layers [52]. Finally, dielectric DBR's (again, nonconducting) have been used for visible wavelengths [53].

As mentioned in the above discussion, AlGaInP VCSEL's have several properties that affect their performance at elevated temperatures. The difficulty in p-type doping, high thermal impedance, and low confinement energies all contribute to a reduction of the output power and device efficiency at high temperatures. Near-infrared VCSEL's have successfully used gain offset to improve high-temperature operation [54]. This concept involves using the property that the gain peak red shifts more with increasing temperature than the lasing mode. By designing the VCSEL such that at room temperature, the gain peak is blue shifted with respect to the lasing mode, one can maximize the elevated temperature range over which sufficiently close alignment between lasing mode and gain peak is maintained.

Fig. 11(a) shows the effect of gain offset in visible-wavelength VCSEL's [49]. The wafer was intentionally grown with some nonuniformity such that from the center to the edge of the wafer the laser mode at room temperature varies from $\lambda = 673$ to 703 nm, while the gain peak remains essentially fixed. By measuring the temperature dependence of the threshold current for VCSEL's at different locations on the wafer, we can study the effects of gain offset. At room temperature, the lowest threshold current, which occurs when the lasing mode and the gain peak are aligned, was obtained for devices emitting at $\lambda \approx 680$ nm. A VCSEL emitting at $\lambda = 675$ nm at room temperature then has the gain peak red shifted with respect to the laser mode. For this device, raising the temperature serves to further increase the separation between the laser mode and the gain peak, resulting in a rapidly increasing threshold current with temperature [dashed curve, Fig. 11(a)]. On the other hand, a VCSEL emitting at $\lambda = 690$ nm at room temperature has the gain peak blue shifted with respect to the laser mode. For this device, the gain peak comes into alignment with the cavity mode as temperature increases, so that initially the threshold current actually decreases with increasing temperature [solid curve, Fig. 11(a)]. Comparison of the solid and dashed curves in Fig. 11(a) shows that although the device with gain offset has a higher threshold current at room temperature, it experiences a smaller variation in the threshold current (<10% for 20 °C $\leq T \leq$ 50 °C). Furthermore, the devices with gain offset also have higher maximum output power [Fig. 11(b)].

In addition to high-temperature operation, a challenge is to demonstrate lasing at shorter ($\lambda < 650$ nm) wavelengths. The standard visible VCSEL structures incorporate approximately 0.5% compressive strain in the $In_{0.56}Ga_{0.44}P$ QW's. To operate at shorter wavelength, one can decrease the In concentration in the QW, which increases its bandgap energy. On the other hand, decreasing the QW In concentration also reduces the compressive strain, which leads to a higher in-plane ground state hole mass and, in turn, a degradation of gain medium performance. Lasing threshold is still achievable at reduced QW In concentration, and edge-emitting lasers with $In_xGa_{1-x}P$ QW's that are tensile strained ($x < 0.52$) have demonstrated lasing in the TM polarization at $\lambda \approx 610$ nm to 640 nm [55]. Unfortunately, it is difficult to achieve lasing threshold with tensile-strained QW's in a VCSEL, because the vertical cavity geometry only allows operation in the lower gain TE polarization.

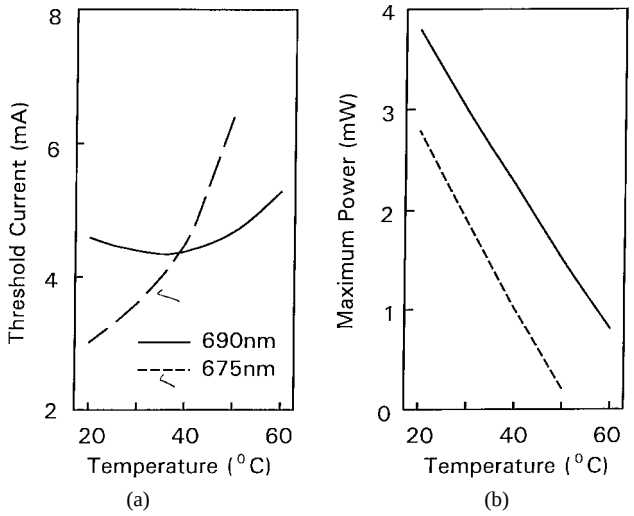


Fig. 11. (a) Threshold current versus temperature for implanted VCSEL's with (solid curve) and without (dashed curve) gain offset. The lasing wavelength at $T = 20$ °C is 690 nm for the former, and 675 nm for the latter. (b) Maximum output power versus temperature for the above VCSEL's.

As an alternative, we explored shortening the emission wavelength by adding aluminum into the QW's, thus using AlGaInP quaternary alloys in both the QW's and the barriers. Numerical simulations involving the effects of varying the amount of aluminum in the QW's show a sharp increase in the threshold current for devices emitting at $\lambda \leq 640$ nm. The main contribution to this high threshold current is current leakage out of the QW region [39]. The onset of current leakage is determined by the QW confinement potential, which at present is limited by the maximum direct bandgap achievable with the AlGaInP barrier layers. Therefore, CW lasing at wavelengths shorter than the 630 nm demonstrated to date is expected to be difficult [56], [57].

## IV. Transverse Electrical and Optical Confinement

Limiting the cross-sectional areas of the electrical current and optical mode effectively in the vicinity of the gain region is important for achieving high efficiency or low threshold current. In Fig. 2, we showed the four device structures presently used for transverse electrical or optical confinement. This section reviews these structures, emphasizing the oxide-confined case, because it presently provides the most effective confinement of both carriers and photons.

### *A. Air-Post Structures*

The simplest method to define the lateral dimensions of a VCSEL cavity is to etch a pillar or post [Fig. 2(a)]. The

first demonstration of a monolithic VCSEL was achieved with an etched air-post structure [58]. Anisotropic dry etching techniques, such as chemically assisted ion beam etching (CAIBE) [59] or reactive ion etching (RIE) [60], make possible the fabrication of pillar structures with small cross-section areas and smooth vertical sidewalls. Strong index guiding is present in an air-post structure because of the large index step at the interface between semiconductor and air. As a result, the lateral dimension of the VCSEL resonator has to be relatively small ($<5$ $\mu$m) if single transverse mode operation is desired [61]. The laser field polarization in an air-post structure is influenced by the shape of the optical cavity cross section [62]. Since it is relatively straightforward to etch asymmetric cross-section air-posts, polarization control is readily achieved in single lasers and in arrays [63].

A disadvantage of the air-post VCSEL is carrier loss due to surface recombination at the side walls. In addition, optical loss increases with greater etch depth and smaller air-post diameter, due to diffraction [64] and scattering from imperfections in the sidewalls [65], respectively. An additional consideration is the high thermal impedance of these structures, due to the absence of an effective heat sink in contact with the laser cavity. As discussed in Section III, a VCSEL is more sensitive to thermal effects than the conventional edge-emitting laser because of the need to align the resonator resonance to the gain spectrum. An important effect of this misalignment is output power "roll over" with increasing injection current [36]. The encapsulation of the air-post structure with a material having high thermal conductance, such as gold, has been successfully used to mitigate high thermal impedance problems [66].

### *B. Ion-Implanted Structures*

A planar VCSEL geometry provides better thermal dissipation as well as simplifies fabrication and packaging. Lateral current confinement is possible in a planar structure through ion implantation [64], [67]–[69]. By selectively implanting ions into a semiconductor material, we can render certain regions insulating and thereby control the flow of the injection current. Different ion species have been used ($O^+$, $N^+$, $F^+$, $H^+$), with protons being the most common. The required implantation energy depends on the ion mass and desired implant depth.

Implanted VCSEL's have demonstrated good reliability [70], [71], in spite of the crystal damage caused by the implanted ions. However, the possibility of active region damage by ions and the indistinct boundary of the implanted region due to lateral scattering of ion species (straggle) limit the proximity of the implanted region to the active layer and the precision with which small apertures can be defined.

Another drawback of ion implantation is that, unlike the air-post structure, it does not provide inherent index guiding for the optical field. Under CW operation, a thermally induced refractive index gradient (thermal lensing) gives rise to index guiding to confine the optical mode [72]. Experimental evidence of thermal lensing comes from the higher threshold currents observed under pulsed operation [73], and from the long time lag observed between electrical modulation and optical response [36], [74]. The index guiding with thermal lensing is insufficient to prevent multilateral-mode operation due to spatial hole burning [75], and the implanted geometry does not provide inherent polarization discrimination or control.

### *C. Regrown Structures*

An approach that provides index guiding in a planar geometry involves using a buried heterostructure [Fig. 2(c)]. Similar to the case in edge emitters, the active region is first isolated by etching away the materials around the intended cavity. Then, the etched regions are replaced with materials that have higher bandgap energies. The regrown regions define the lateral boundaries of the active region and contribute to electrical as well as optical confinement, because of their wider bandgaps and lower refractive indices.

The epitaxial regrowth is quite challenging for VCSEL's because it typically requires growth on highly reactive AlGaAs surfaces. Careful etching techniques combined with special cleaning processes and/or avoiding atmospheric exposure are necessary. Three successfully demonstrated regrowth techniques to date are: etching followed by liquid phase epitaxy (LPE) utilizing melt-back cleaning [76], [77]; vacuum integrated dry etching and molecular beam epitaxy (MBE) [78], [79]; and dry etching followed by chemical pretreatments before metalorganic vapor phase epitaxy (MOVPE) [80].

Conventional index-guided [81] and antiguided [82] VCSEL's fabricated with the above regrowth techniques have demonstrated reliable single-mode operation. Regrowth allows implementation of a variety of device schemes for channeling the flow of current, such as lateral current injection. It can also be used to passivate the cavity sidewall, restore heat sinking material for thermal dissipation [78], or incorporate optimized epilayers for microelectronic device integration [83].

### *D. Oxide-Confined VCSEL*

Many recent advances in VCSEL performance are due to the use of selective oxidation to provide index guiding and electrical confinement [Fig. 2(d)]. Wet oxidation of AlGaAs [84], [85], which was successfully implemented in edge emitters [86]–[88], produces highly effective current apertures in hybrid VCSEL's operating with dielectric DBR's [6], as well as in monolithic VCSEL's operating with semiconductor DBR's [89]. Significant improvements in laser performance have been reported for VCSEL's operating at 980, 850, 780, and 650 nm.

The implementation of selective oxidation is relatively straightforward [89], [90]. One begins by growing Al-rich AlGaAs layers at the desired locations of the current apertures. This is particularly amendable for a VCSEL due to the typical presence of high Al-content epilayers. For lateral oxidation of the Al-rich layers to occur, a mesa structure is formed by etching to expose the sidewalls. Placing the mesa structure in a steam environment at temperatures of 350 °C to 500 °C converts the AlGaAs to a robust insulating oxide with low refractive index [85]. The oxidation starts at the exposed surfaces at the mesa sidewall and propagates toward the center, resulting in an unoxidized aperture surrounded by oxidized material, as shown in Fig. 12. Because the oxidation rate is proportional to the Al concentration [89], the aperture is

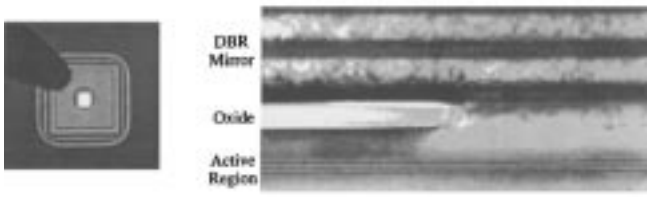


(a) (b)

Fig. 12. Current aperture of selectively oxidized VCSEL: (a) top view of laser mesa showing square oxide aperture, (b) transmission electron cross-section image of selectively oxidized VCSEL showing oxide aperture above the active region [91].

the smallest in the layer with the highest Al concentration. The confinement layers can be located significantly closer to the gain layer than in the other VCSEL structures shown in Fig. 2. This mitigates lateral carrier diffusion effects, resulting in highly effective current confinement in the active layer, especially for small apertures.

The temperature dependence of the oxidation rates of AlGaAs alloys follow an Arrhenius relationship. A strong compositional dependence of the oxidation rates results from the compositional dependence of the activation energies. Fig. 13 shows that the measured oxidation rate of $Al_xGa_{1-x}As$ changes by more than two orders of magnitude for $0.82 \leq x \leq 1$ [89]. Thus, a high degree of oxidation selectivity between AlGaAs layers can be obtained with minute compositional differences between layers. On the other hand, this also means that stringent compositional control between layers and uniformity within a layer are critical during growth. At Sandia National Laboratories, the VCSEL wafers are grown by MOVPE, which is especially suited for oxide-confined VCSEL growth because of the complete accessibility of the AlGaAs alloy range, the stringent compositional control, and the high degree of compositional uniformity [91]. For the low-refractive-index DBR layers not intended for oxidation, we use a GaAs mole fraction of 6%–8%. For the low-refractive-index layers intended for oxidation, the GaAs mole fraction is adjusted to 2% to increase their oxidation rate. The oxide layers contain a small amount of Ga, which we find leads to isotropic oxidation and laser structures which are mechanically stable to thermal cycling [92].

The buried oxide has a significantly lower refractive index ($n \simeq 1.6$) than the original semiconductor layer [87]. Thus, the oxide can also be used in DBR's to give high index contrast [93], [57]. The lower index oxide surrounding the unoxidized current aperture also provides strong index guiding to the laser field [74], [94], [95]. The induced effective index difference between the cavity and the surrounding region containing the oxide layer [96] can be controlled through the thickness of the oxide layer and the position of the oxide layer(s) relative to the optical cavity [97]. Positioning the oxide layers directly adjacent to or even inside the optical cavity produces the strongest index confinement. However, the abrupt index discontinuity of the oxide layer will induce optical loss for cavity diameters $<5$ $\mu$m, as shown in Fig. 9.

Another novel optical effect arising from the reduced index of the buried oxide aperture is illustrated in Fig. 14 [97].

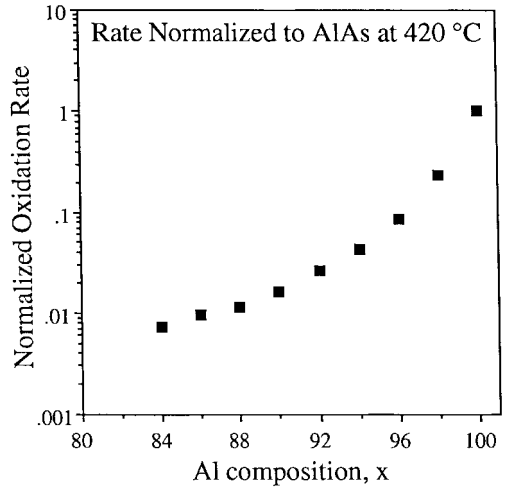


Fig. 13. Measured oxidation rate of $Al_xGa_{1-x}As$ versus Al composition, $x$.

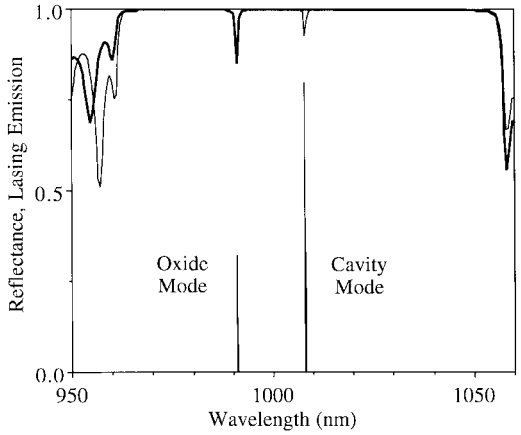


Fig. 14. The calculated DBR reflectance containing an oxidized layer (heavy curve) or an unoxidized layer (light curve); superimposed is the observed lasing emission showing both oxide and cavity modes.

In the region of the optical cavity under the oxide layer(s), the longitudinal cavity resonance is strongly modified relative to the as-grown cavity resonance. Plotted in Fig. 14 is the calculated reflectance of two cavities, one with the top DBR containing a single oxide layer next to the active region and the other with an unoxidized as-grown layer. The reflectivity across the stopband in Fig. 14 is increased for the DBR containing the oxide layer and the cavity resonance is blue-shifted relative to the unoxidized cavity resonance wavelength. Superimposed on Fig. 14 is the observed lasing spectrum from a VCSEL which exhibits two simultaneous lasing emission separated by 17 nm. The shorter wavelength emission corresponds to lasing modes at the periphery of the current aperture ("oxide" modes) arising from carriers diffusing in the QW's under the oxide layer, while the cavity modes inside the aperture emit at the as-grown resonance wavelength. The lasing emission of the oxide modes can be tailored through the thickness and position of the buried oxide aperture(s) [97]. For example, using quarterwave-thick oxide layers on each side of the optical cavity [90] sufficiently shifts the resonance of these modes off of the DBR stopband to inhibit them from lasing.

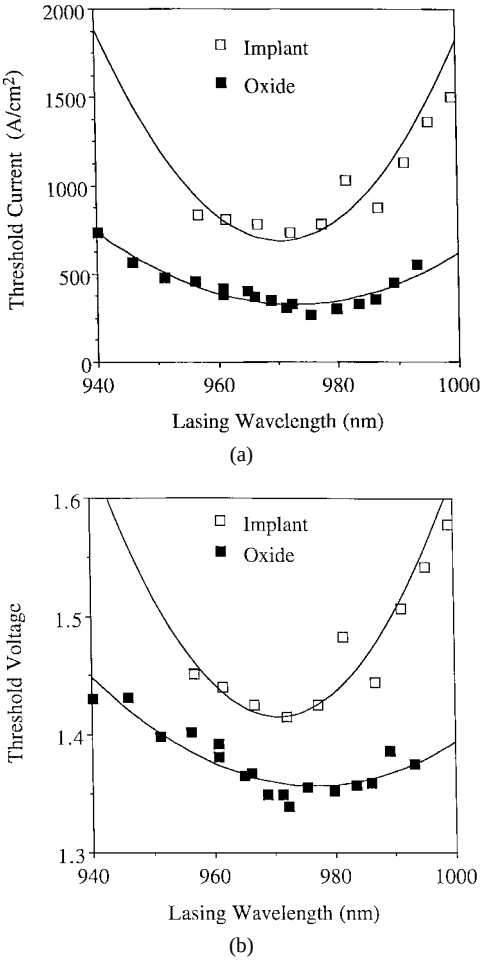


Fig. 15. Characteristics for broad-area selectively oxidized and implanted VCSEL's fabricated from the same wafer. (a) Threshold current density. (b) Threshold voltage.

Fig. 15 compares the threshold voltage and current density, $V_{\rm th}$ and $J_{\rm th}$, respectively, for broad-area oxide-confined and implanted 970-nm VCSEL's, fabricated from the same wafer [97]. The superior threshold properties of the oxide-confined devices are evident, in terms of overall lower threshold current densities and voltages. Also, they operate over a wider wavelength range, which translates to a wider temperature operating range. Monolithic oxide-confined IR VCSEL's now hold several performance records. They include: 1) lowest threshold current of $<10$ $\mu$A [7], which is lower than any other diode laser; 2) lowest threshold voltage, $<1.33$ V at 970 nm [89]; 3) highest power conversion efficiency of $>50\%$ [4], which is competitive with the best edge emitters; and 4) highest small-signal modulation bandwidth of $>20$ GHz [98].

Selective oxidization also results in higher performance for visible-wavelength VCSEL's, giving threshold currents and voltages less than 1 mA and 2 V, respectively [56]. Also demonstrated are CW emission down to 642 nm and power conversion efficiency $>10\%$ [56]. As the DBR's for the 640–690-nm wavelength range are composed of AlGaAs alloys, the design to enable selective oxidation is similar to that for the near-IR. In Fig. 16, we show a comparison of threshold current across a wafer for oxidized and implanted broad-area AlGaInP VCSEL's. Similar to the near-IR VCSEL's (Fig. 15),

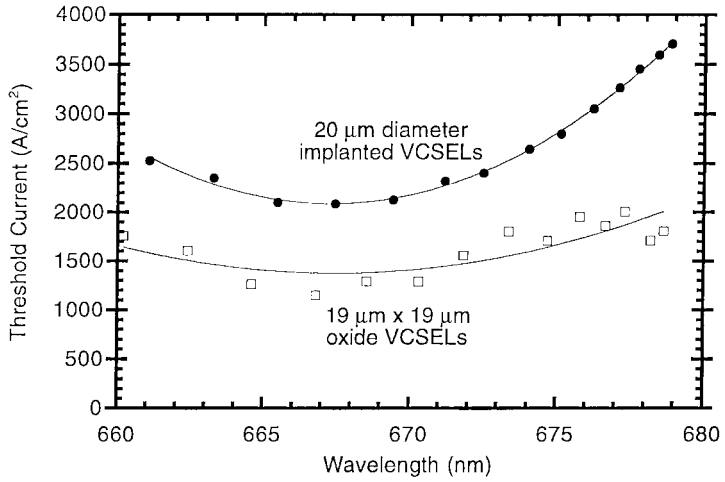


Fig. 16. Threshold current density versus wavelength for selectively oxidized and implanted visible-wavelength VCSEL's.

the oxidized devices have clearly lower threshold currents than the implanted ones from the same wafer. The lower electrical power requirement for the oxide VCSEL's is particularly relevant toward achieving short wavelength operation, where current leakage is expected to be significant because of low QW confinement potentials.

## V. Conclusion

This paper discusses the design, fabrication, and performance of vertical-cavity surface-emitting lasers (VCSEL's). We emphasize monolithic structures, where graded-index semiconductor distributed Bragg reflectors provide high reflectivity and low electrical resistance. Because the longitudinal modes of a short high-$Q$ VCSEL resonator are well defined and widely spaced in frequency, laser behavior is sensitive to the overlap of these modes with the gain spectrum. For current injection devices, the gain region typically consists of QW's. The wide variety of gain region materials, together with the degrees of freedom provided by quantum confinement and strain allow VCSEL operation at wavelengths ranging from near-IR to visible. The development of phosphide-based VCSEL's operating at visible wavelengths represents an important advance. Progress in the design and performance of AlGaInP-based VCSEL's make viable their use in applications ranging from bar-code scanners to plastic-fiber-based optical links. The development efforts in near-IR and visible VCSEL's are aided by the availability of microscopic VCSEL models that accurately describe the band structure influences, as well as wavelength and carrier density dependences. These models are used extensively in the analyses of experimental data, resulting in the understanding and optimization of gain region properties, especially those relating to lasing threshold. Finally, important to VCSEL performance is effective transverse electrical and optical confinement. Many of the recent breakthroughs, such as $>50\%$ wall-plug efficiency and $<100$-$\mu$A threshold current, are due to the use of selective oxidation to provide current confinement and index guiding. The technique is very versatile, leading to improvements in VCSEL performance in GaAs, InGaAs,

InGaAsP, and AlGaInP systems, and is applicable to both monolithic VCSEL's operating with semiconductor DBR's as well as hybrid VCSEL's operating with dielectric DBR's.

After more than a decade of research and development that cumulated in the device performance discussed in this paper, the VCSEL appears ready for high volume and potentially low-cost manufacture. The first applications being considered are those requiring low drive powers, for example, in optical data links. Also being proposed are more advanced schemes involving parallel multigigabit/second data links with free-space or holographic interconnections, for extremely high (terabit/second) aggregate data rates [99]. Other commercial applications under development include compact disk optical heads, copier printer heads, optical scanners, projection systems, and optical displays.

Ongoing research and development efforts are directed toward addressing aspects of VCSEL performance that may be relevant for future applications. A need in many potential applications is higher output power, especially into the fundamental optical mode. One promising approach to high-power fundamental mode operation in a VCSEL or VCSEL array involves the use of "antiguided" or "leaky" modes [100], [101]. Extending VCSEL operation to longer (2–10 $\mu$m) as well as shorter wavelengths (e.g., $<$550 nm) are of interest because of spectroscopic and sensor applications in the former and optical display applications in the latter. Integration of the VCSEL with microelectronics and microoptics is being implemented to increase functionality [83], [102]. Work is continuing to increase modulation bandwidth and to further reduce lasing threshold current. There are also ongoing efforts to demonstrate the ability of the VCSEL to function under environmental conditions that are likely in commercial or military applications. An important challenge involves the transition of the advanced designs, epitaxial structures, and requisite fabrication technologies into robust manufacturing platforms. If successful, the VCSEL will likely play a defining role in the optoelectronic industry.

## ACKNOWLEDGMENT

Many individuals have contributed to the VCSEL research at Sandia National Laboratories. The authors are especially grateful for collaborations with R. P. Schneider, Jr., and H. Q. Hou. The authors would also like to acknowledge the technical contributions of J. Figiel, K. Geib, R. Hickman, S. Kilcoyne, J. Nevers, A. Owyoung, and S. Samora. Sandia is a multiprogram laboratory operated by Sandia Corporation, a Lockheed Martin Company, for the U.S. Department of Energy.

## REFERENCES

[1] H. Soda, K. Iga, C. Kitahara, and Y. Suematsu, "GaInAsP/InP surface emitting injection lasers," *Jpn. J. Appl. Phys.*, vol. 18, pp. 2329–2330, 1979.

[2] K. Iga, S. Ishikawa, S. Ohkouchi, and T. Nishimura, "Room-temperature pulsed oscillation of GaAlAs/GaAs surface-emitting injection laser," *Appl. Phys. Lett.*, vol. 45, pp. 348–350, 1984.

[3] F. Koyama, S. Kinoshita, and K. Iga, "Room-temperature continuous wave lasing characteristics of GaAs vertical cavity surface-emitting lasers," *Appl. Phys. Lett.*, vol. 55, pp. 221–222, 1989.

[4] K. L. Lear, K. D. Choquette, R. P. Schneider, Jr., S. P. Kilcoyne, and K. M. Geib, "Selectively oxidized vertical-cavity surface emitting lasers with 50% power conversion efficiency," *Electron. Lett.*, vol. 31, pp. 208–209, 1995.

[5] B. Weigl, M. Grabherr, G. Reiner, and K. J. Ebeling, "High efficiency selectively oxidised MBE grown vertical-cavity surface-emitting lasers," *Electron. Lett.*, vol. 32, pp. 557–558, 1996.

[6] D. L. Huffaker, D. G. Deppe, K. Kumar, and T. J. Rogers, "Native-oxide defined ring contact for low threshold vertical-cavity lasers," *Appl. Phys. Lett.*, vol. 65, pp. 97–99, 1994.

[7] M. H. MacDougal, P. D. Dapkus, V. Pudikov, H. Zhao, and G. M. Yang, "Ultralow threshold current vertical-cavity surface emitting lasers with AlAs-oxide-GaAs distributed Bragg reflectors," *IEEE Photon. Technol. Lett.*, vol. 7, pp. 229–231, 1995.

[8] Y. Hayashi, T. Mukaihara, N. Hatori, N. Ohnoki, A. Matsutani, F. Koyama, and K. Iga, "Record low-threshold index-guided InGaAs/GaAlAs vertical-cavity surface-emitting laser with a native oxide confinement structure," *Electron. Lett.*, vol. 31, pp. 560–561, 1995.

[9] C. Lei, T. J. Rogers, D. G. Deppe, and B. G. Streetman, "ZnSe/$CaF_2$ quarter-wave Bragg reflector for the vertical-cavity surface-emitting laser," *J. Appl. Phys.*, vol. 69, pp. 7430–7434, 1991.

[10] P. L. Gourley and T. J. Drummond, "Single crystal, epitaxial multilayers of AlAs, GaAs, and $Al_xGa_{1-x}As$ for use as optical interferometric elements," *Appl. Phys. Lett.*, vol. 49, pp. 489–491, 1986.

[11] J. L. Jewell, Y. H. Lee, S. L. McCall, J. P. Harbison, and L. T. Florez, "High-finesse (Al, Ga)As interference filters grown by molecular beam epitaxy," *Appl. Phys. Lett.*, vol. 53, pp. 640–642, 1988.

[12] J. J. Dudley, D. I. Babić, R. Mirin, L. Yang, B. I. Miller, R. J. Ram, T. Reynolds, E. L. Hu, and J. E. Bowers, "Low threshold, wafer fused long wavelength vertical cavity lasers," *Appl. Phys. Lett.*, vol. 64, pp. 1463–1465, 1994.

[13] M. Sugimoto, H. Kosaka, K. Kurihara, I. Ogura, T. Numai, and K. Kasahara, "Very low threshold current density in vertical-cavity surface-emitting laser diodes with periodically doped distributed Bragg reflectors," *Electron. Lett.*, vol. 28, pp. 385–387, 1992.

[14] K. Kojima, R. A. Morgan, T. Mullaly, G. D. Guth, M. W. Focht, R. E. Leibenguth, and M. T. Asom, "Reduction of p-doped mirror electrical resistance of GaAs/AlGaAs vertical-cavity surface-emitting lasers by delta doping," *Electron. Lett.*, vol. 29, pp. 1771–1772, 1993.

[15] M. G. Peters, B. J. Thibeault, D. B. Young, J. W. Scott, F. H. Peters, A. C. Gossard, and L. A. Coldren, "Band-gap engineered digital alloy interfaces for lower resistance vertical-cavity surface-emitting lasers," *Appl. Phys. Lett.*, vol. 63, pp. 3411–3413, 1993.

[16] K. Tai, L. Yang, Y. H. Wang, J. D. Wynn, and A. Y. Cho, "Drastic reduction of series resistance in doped semiconductor distributed Bragg reflectors for surface-emitting lasers," *Appl. Phys. Lett.*, vol. 56, pp. 2496–2498, 1990.

[17] M. Hong, J. P. Mannaerts, J. M. Hong, R. J. Fischer, K. Tai, J. Kwo, J. M. Vandenberg, Y. H. Wang, and J. Gamelin, "A simple way to reduce series resistance in p-doped semiconductor distributed Bragg reflectors," *J. Cryst. Growth*, vol. 111, pp. 1071–1075, 1991.

[18] S. A. Chalmers, K. L. Lear, and K. P. Killeen, "Low resistance wavelength-reproducible p-type (Al, Ga)As distributed Bragg reflectors grown by molecular beam epitaxy," *Appl. Phys. Lett.*, vol. 62, pp. 1585–1587, 1993.

[19] K. L. Lear and R. P. Schneider, Jr., "Uniparabolic mirror grading for vertical cavity surface emitting lasers," *Appl. Phys. Lett.*, vol. 68, pp. 605–607, 1996.

[20] K. L. Lear, R. P. Schneider, K. D. Choquette, S. P. Kilcoyne, J. J. Figiel, and J. C. Zolper, "Vertical cavity surface emitting lasers with 21% efficiency by metalorganic vapor phase epitaxy," *IEEE Photon. Technol. Lett.*, vol. 6, pp. 1053–1055, 1994.

[21] K. L. Lear, S. P. Kilcoyne, and S. A. Chalmers, "High power conversion efficiencies and scaling issues for multimode vertical-cavity top-surface-emitting lasers," *IEEE Photon. Tech. Lett.*, vol. 6, pp. 778–781, 1994.

[22] K. L. Lear, S. A. Chalmers, and S. P. Kilcoyne, "Effects of implant annealing on the power conversion efficiency of vertical cavity top-surface emitting lasers," in *Proc. LEOS'93*, San Jose, CA, 1993, pp. 546–547.

[23] S. W. Corzine, R. S. Geels, J. W. Scott, R.-H. Yan, and L. A. Coldren, "Design of Fabry–Perot surface-emitting lasers with a periodic gain structure," *IEEE J. Quantum Electron.*, vol. 25, pp. 1513–1524, 1989.

[24] D. Ahn and S. L. Chuang, "Optical gain in a strained-layer quantum well laser," *IEEE J. Quantum Electron.*, vol. 24, pp. 2400–2406, 1988.

[25] S. W. Corzine, R.-H. Yan, and L. A. Coldren, "Optical gain in III–V bulk and quantum well semiconductors," in *Quantum Well Lasers*, P. S. Zory, Jr., Ed. New York: Academic, 1993. ch. 4.

[26] W. W. Chow, S. W. Koch, and M. Sargent, III, *Semiconductor-Laser Physics*. Berlin: Germany: Springer-Verlag, 1994.

[27] R. Jin, D. Boggavarapu, G. Khitrova, H. M. Gibbs, Y. Z. Hu, S. W. Koch, and N. Peyghambarian, "Linewidth broadening factor of a microcavity semiconductor laser," *Appl. Phys. Lett.*, vol. 61, pp. 1883–1885, 1992.

[28] Y. H. Lee, A. Chavez-Pirson, S. W. Koch, H. M. Gibbs, S. H. Park, J. Morhange, A. Jeffery, N. Peyghambarian, L. Banyai, A. C. Gossard, and W. Wiegmann, "Room-temperature optical nonlinearities in GaAs," *Phys. Rev. Lett.*, vol. 57, pp. 2446–2449, 1986.

[29] M. Hofmann, M. Koch, J. Feldmann, W. Elsäßer, E. O. Göbel, W. W. Chow, and W. W. Koch, "Picosecond gain dynamics of an actively mode-locked external-cavity laser diode," *IEEE J. Quantum Electron.*, vol. 30, pp. 1756–1762, 1994.

[30] W. E. Lamb, Jr., "Theory of an optical maser," *Phys. Rev. A*, vol. 134, pp. 1429–1450, 1964.

[31] W. W. Chow, R. P. Schneider, Jr., J. A. Lott, and K. D. Choquette, "Wavelength dependence of the threshold in an InGaP-InAlGaP vertical cavity surface emitting laser," *Appl. Phys. Lett.*, vol. 65, pp. 135–137, 1994.

[32] W. W. Chow, S. W. Corzine, D. B. Young, and L. A. Coldren, "Many-body effects in the temperature dependence of threshold in a VCSEL," *Appl. Phys. Lett.*, vol. 66, pp. 2460–2462, 1995.

[33] K. D. Choquette, W. W. Chow, M. H. Crawford, K. M. Geib, and R. P. Schneider, Jr., "Threshold investigation of oxide-confined vertical-cavity laser diodes," *Appl. Phys. Lett.*, vol. 68, pp. 3689–3691, 1996.

[34] H. Haug and S. W. Koch, *Quantum Theory of the Optical and Electronic Properties of Semiconductors*, 3rd ed. Singapore: World Scientific, 1994.

[35] J. M. Luttinger and W. Kohn, "Motion of electrons and holes in perturbed periodic fields," *Phys. Rev.*, vol. 97, pp. 869–883, 1955.

[36] G. Hasnain, K. Tai, L. Yang, Y. H. Wang, R. J. Fischer, J. D. Wynn, B. Weir, N. K. Dutta, and A. Y. Cho, "Performance of gain-guided surface emitting lasers with semiconductor distributed Bragg reflectors," *IEEE J. Quantum Electron.*, vol. 27, pp. 1377–1385, 1991.

[37] O. Madelung, Ed., *Landolt-Bornstein Numerical Data and Functional Relationships in Science and Technology*. Berlin: Springer-Verlag, 1982, group III, vol. 17a.

[38] S. Adachi, *Physical Properties of III–V Semiconductor Compunds*. New York: Wiley, 1992.

[39] W. W. Chow, M. H. Crawford, and R. P. Schneider, Jr., "Minimization of threshold current in short wavelength AlGaInP vertical-cavity surface-emitting lasers," *IEEE J. Select. Topics Quantum Electron.*, vol. 1, pp. 649–653, 1995.

[40] K. D. Choquette, W. W. Chow, G. R. Hadley, H. Q. Hou, and K. M. Geib, "Scalability of small-aperture selectively oxidized vertical-cavity surface-emitting lasers," *Appl. Phys. Lett.*, vol. 70, pp. 823–825, 1997.

[41] E. R. Hegblom, D. I. Babic, B. J. Thibeault, and L. A. Coldren, "Estimation of scattering losses in dielectrically apertured vertical cavity lasers," *Appl. Phys. Lett.*, vol. 68, pp. 1757–1759, 1996.

[42] R. P. Schneider, Jr., J. A. Lott, M. H. Crawford, and K. D. Choquette, "Epitaxial design and performance of AlGaInP red (650–690 nm) VCSEL's," *Int. J. High Speed Electron. Systems*, vol. 5, pp. 625–666, 1994.

[43] B. Tell, R. E. Leibenguth, K. F. Brown-Goebeler, and G. Livescu, "Short wavelength (699 nm) electrically pumped vertical-cavity surface-emitting lasers," *IEEE Photon. Technol. Lett.*, vol. 4, pp. 1195–1196, 1992.

[44] T. E. Sale, J. S. Roberts, J. Woodhead, J. P. R. David, and P. N. Robson, "Room temperature visible (683–713 nm) all-AlGaAs vertical-cavity surface-emitting lasers (VCSEL's)," *IEEE Photon. Technol. Lett.*, vol. 8, pp. 473–475, 1996.

[45] J. A. Lott and R. P. Schneider, Jr., "Electrically injected visible (639–661 nm) vertical cavity surface emitting laser," *Electron. Lett.*, vol. 29, pp. 830–832, 1993.

[46] K. Tai, K.-F. Huang, C.-C. Wu, and J. Wynn, "Visible InGaP/InGaAlP quantum well top surface emitting laser diodes," *Appl. Phys. Lett.*, vol. 63, pp. 2732–2734, 1993.

[47] J. A. Lott, R. P. Schneider, Jr., K. D. Choquette, S. P. Kilcoyne, and J. J Figiel, "Room temperature continuous wave operation of red vertical cavity surface emitting laser diodes," *Electron. Lett.*, vol. 29, pp. 1693–1694, 1993.

[48] M. H. Crawford, R. P. Schneider, Jr., K. D. Choquette, K. L. Lear, S. P. Kilcoyne, and J. J. Figiel, "High efficiency AlGaInP based 660–680 nm vertical-cavity surface emitting lasers," *Electron. Lett.*, vol. 31, pp. 196–197, 1995.

[49] M. H. Crawford, R. P. Schneider, Jr., K. D. Choquette, and K. L. Lear, "Temperature-dependent characteristics and single-mode performance of AlGaInP-based 670–690 nm vertical-cavity surface emitting lasers," *IEEE Photon. Technol. Lett.*, vol. 7, pp. 724–725, 1995.

[50] J. S. Nelson, E. D. Jones, S. M. Meyers, D. M. Follstaedt, H. P. Hjalmarson, J. E. Schirber, R. P. Schneider, Jr., J. E. Foquet, V. M. Robbins, and K. W. Carey, "Compositional dependence of the luminescence of $In_{0.49}(Al_yGa_{1-y})_{0.51}P$ alloys near the direct-indirect band-gap crossover," *Phy. Rev. B*, vol. 53, pp. 15893–15901, 1996.

[51] R. P. Schneider, Jr., and J. A. Lott, "InAlP/InAlGaP distributed Bragg reflectors for visible vertical cavity surface-emitting lasers," *Appl. Phys. Lett.*, vol. 62, pp. 2748–2750, 1993.

[52] M. H. MacDougal, S. G. Hummel, P. D. Dapkus, H. Zhao, and Y. Cheng, "Epitaxial (Al, Ga)InP-oxide distributed Bragg reflectors for use in visible-wavelength optical devices," *IEEE Photon. Technol. Lett.*, vol. 7, pp. 385–387, 1995.

[53] J. A. Lott, R. P. Schneider, Jr., and K. J. Malloy, "Partial top dielectric stack distributed Bragg reflectors for red vertical cavity surface emitting laser arrays," *IEEE Photon. Technol. Lett.*, vol. 6, pp. 1397–1399, 1994.

[54] D. B. Young, J. W. Scott, M. G. Peters, M. L. Majewski, B. J. Thibeault, S. W. Corzine, and L. A. Coldren, "Enhanced performance of offset-gain high-barrier vertical-cavity surface-emitting lasers," *IEEE J. Quantum Electron.*, vol. 29, pp. 2013–2021, 1993.

[55] T. Tanaka, H. Yanagisawa, and S. Minagawa, "Comparison between tensile-strained AlGaInP SQW and MQW LD's emitting at 615 nm," *Electron. Lett.*, vol. 30, pp. 566–568, 1994.

[56] K. D. Choquette, R. P. Schneider, Jr., M. H. Crawford, K. M. Geib, and J. J. Figiel, "Continuous wave operation of 640–660 nm selectively oxidized AlGaInP vertical-cavity lasers," *Electron. Lett.*, vol. 31, pp. 1145–1146, 1995.

[57] J. A. Lott, L. V. Buydens, K. J. Malloy, K. Kobayashi, and S. Ishikawa, "Visible (630–650 nm) vertical cavity surface emitting lasers with Al-oxide/AlGaInP distributed Bragg reflectors," *Inst. Phys. Conf. Ser.*, 1996, vol. 145, pp 973–976.

[58] J. L. Jewell, A. Sherer, S. L. McCall, Y. H. Lee, S. Walker, J. P. Harbison, and L. T. Florez, "Low-threshold electrically pumped vertical-cavity surface-emitting microlasers," *Electron. Lett.*, vol. 25, pp. 1123–1124, 1989.

[59] A. Sherer, J. L. Jewell, Y. H. Lee, J. P. Harbison, and L. T. Florez, "Fabrication of microlasers and microresonator optical switches," *Appl. Phys. Lett.*, vol. 55, pp. 2724–2723, 1989.

[60] R. S. Geels, S. W. Corzine, J. W. Scott, D. B. Young, and L. A. Coldren, "Low threshold planarized vertical-cavity surface-emitting lasers," *IEEE Photon. Technol. Lett.*, vol. 2, pp. 234–236, 1990.

[61] C. J. Chang-Hasnain, M. Orenstein, A. Von Lehmen, L. T. Florez, J. P. Harbison, and N. G. Stoffel, "Transverse mode characteristics of vertical-cavity surface-emitting lasers," *Appl. Phys. Lett.*, vol. 57, pp. 218–220, 1990.

[62] K. D. Choquette and R. E. Leibenguth, "Control of vertical-cavity surface-emitting laser polarization with anisotropic transverse cavity geometries," *IEEE Photon. Technol. Lett.*, vol. 6, pp. 40–42, 1994.

[63] T. Yoshikawa, H. Kosaka, K. Kurihara, M. Kajita, Y. Sugimoto, and K. Kasahara, "Complete polarization control of $8 \times 8$ vertical-cavity surface-emitting laser matrix arrays," *Appl. Phys. Lett.*, vol. 66, pp. 908–910, 1995.

[64] Y. H. Lee, J. L. Jewell, B. Tell, K. F. Brown-Goebeler, A. Sherer, J. P. Harbison, and L. T. Florez, "Effects of etch depth and ion implantation on surface emitting microlasers," *Electron. Lett.*, vol. 26, pp. 225–227, 1990.

[65] B. J. Thibeault, T. A. Strand, T. Wipiejewski, M. G. Peters, D. B. Young, S. W. Corzine, and L. A. Coldren, "Evaluating the effects of optical and carrier losses in etched-post vertical cavity lasers," *J. Appl. Phys.*, vol. 78, pp. 5871–5875, 1995.

[66] K. D. Choquette, G. Hasnain, J. P. Mannaerts, J. D. Wynn, R. C. Wetzel, M. Hong, R. S. Freund, and R. E. Leibenguth, "Vertical-cavity surface-emitting lasers fabricated by vacuum integrated processing," *IEEE Photon. Technol. Lett.*, vol. 4, pp. 951–954, 1992.

[67] K. Tai, R. J. Fischer, K. W. Wang, S. N. G. Chu, and A. Y. Cho, "Use of implant isolation for fabrication of vertical-cavity surface-emitting laser diodes," *Electron. Lett.*, vol. 25, pp. 1644–1645, 1989.

[68] M. Orenstein, A. Von Lehmen, C. J. Chang-Hasnain, N. G. Stoffel, J. P. Harbison, L. T. Florez, E. Clausen, and J. E. Jewell, "Vertical-cavity surface-emitting InGaAs/GaAs lasers with planar lateral definition," *Appl. Phys. Lett.*, vol. 56, pp. 2384–2386, 1990.

[69] Y. H. Lee, B. Tell, K. F. Brown-Goebeler, and J. L. Jewell, "Top-surface-emitting GaAs four-quantum-well lasers emitting at 0.85 $\mu$m," *Electron. Lett.*, vol. 26, pp. 710–711, 1990.

[70] C. C. Wu, K. Tai, T. C. Huang, and K. F. Huang, "Reliability studies of gain-guided 0.85 $\mu$m GaAs/AlGaAs quantum well surface emitting lasers," *IEEE Photon. Technol. Lett.*, vol. 6, pp. 37–39, 1994.

[71] J. K. Guenter, R. A. Hawthorne, III, and D. N. Granville, "Reliability of proton-implanted VCSEL's for data communications," in *Proc. SPIE*, 1996, vol. 2683, pp. 102–113.
[72] G. R. Hadley, K. L. Lear, M. E. Warren, K. D. Choquette, J. W. Scott, and S. W. Corzine, "Comprehensive numerical modeling of vertical-cavity surface-emitting lasers," *IEEE J. Quantum Electron.*, vol. 32, pp. 607–616, 1996.
[73] N. K. Dutta, L. W. Tu, G. Hasnain, G. Zydzik, Y. H. Wang, and A. Y. Cho, "Anomalous temporal response of gain guided surface emitting lasers," *Electron. Lett.*, vol. 27, pp. 208–210, 1991.
[74] K. L. Lear, R. P. Schneidner, Jr., K. D. Choquette, and S. P. Kilcoyne, "Index guiding dependent effects in implant and oxide confined vertical-cavity lasers," *IEEE Photon. Technol. Lett.*, vol. 8, pp. 740–742, 1996.
[75] D. Vakhshoori, J. D. Wynn, G. J. Aydzik, R. E. Leibenguth, M. T. Asom, K. Kojima, and R. A. Morgan, "Top-surface emitting lasers with 1.9 V threshold voltage and the effect of spatial hole burning on their transverse mode operation and efficiencies," *Appl. Phys. Lett.*, vol. 62, pp. 1448–1450, 1993.
[76] S. Kinoshita and K. Iga, "Circular buried heterostructure (CBH) GaAlAs/GaAs surface emitting lasers," *IEEE J. Quantum Electron.*, vol. 23, pp. 882–888, 1987.
[77] M. Ogura, S. Mukai, M. Shimada, T. Asaka, Y. Yamasaki, T. Seki, and H. Iwano, "Surface-emitting laser diode with distributed Bragg reflector and buried heterostructure," *Electron. Lett.*, vol. 26, pp. 18–19, 1990.
[78] K. D. Choquette, M. Hong, R. S. Freund, J. P. Mannaerts, R. C. Wetzel, and R. E. Leibenguth, "Vertical-cavity surface-emitting laser diodes by *in situ* dry etching and molecular beam epitaxial regrowth," *IEEE Photon. Technol. Lett.*, vol. 5, pp. 284–287, 1993.
[79] M. Hong, D. Vakhshoori, L. H. Grober, J. P. Mannaerts, M. T. Asom, J. D. Wynn, F. A. Thiel, and R. S. Freund, "Buried heterostructure laser diodes fabricated by *in situ* processing," *J. Vac. Sci. Technol. B*, vol. 12, pp. 1258–1261, 1994.
[80] C. J. Chang-Hasnain, Y. A. Wu, G. S. Li, G. Hasnain, K. D. Choquette, C. Caneau, and L. T. Florez, "Low threshold buried heterostructure vertical cavity surface emitting laser," *Appl. Phys. Lett.*, vol. 63, pp. 1307–1309, 1993.
[81] K. Mori, T. Asaka, H. Iwano, M. Ogura, S. Fujii, T. Okada, and S. Mukai, "Effect of cavity size on lasing characteristics of a distributed Bragg reflector-surface emitting laser with buried heterostructure," *Appl. Phys. Lett.*, vol. 60, pp. 21–22, 1992.
[82] Y. A. Wu, G. S. Li, R. F. Nabiev, K. D. Choquette, C. Caneau, and C. J. Chang-Hasnain, "Single-mode, passive antiguide vertical cavity surface emitting laser," *IEEE J. Select. Topics Quantum Electron.*, vol. 1, pp. 629–637, 1995.
[83] P. Zhou, J. Cheng, J. C. Zolper, K. L. Lear, S. A. Chalmers, G. A. Vawter, R. E. Leibenguth, and A. C. Adams, "Monolithic optoelectronic switch based on the integration of a GaAs/AlGaAs heterojunction bipolar transistor and a GaAs vertical-cavity surface-emitting laser," *IEEE Photon. Technol. Lett.*, vol. 5, pp. 1035–1038, 1993.
[84] W. T. Tsang, "Self-terminating thermal oxidation of AlAs epilayers grown on GaAs by molecular beam epitaxy," *Appl. Phys. Lett.*, vol. 33, pp. 426–429, 1978.
[85] J. M. Dallesasse, N. Holonyak, Jr., A. R. Sugg, T. A. Richard, and N. El-Zein, "Hydrolyzation oxidation of $Al_xGa_{1-x}As$-AlAs-GaAs quantum well heterostructures and superlattices," *Appl. Phys. Lett.*, vol. 57, pp. 2844–2846, 1990.
[86] J. M. Dallesasse and N. Holonyak, Jr., "Native-oxide stripe-geometry $Al_xGa_{1-x}As$-GaAs quantum well heterostructure lasers," *Appl. Phys. Lett.*, vol. 58, pp. 394–396, 1991.
[87] F. A. Kish, S. J. Caracci, N. Holonyak, Jr., J. M. Dallesasse, K. C. Hsieh, M. J. Ries, S. C. Smith, and R. D. Burnham, "Planar native-oxide index-guided $Al_xGa_{1-x}As$-GaAs quantum well heterostructure lasers," *Appl. Phys. Lett.*, vol. 59, pp. 1755–1757, 1991.
[88] S. A. Maranowski, A. R. Sugg, E. I. Chen, and N. Holonyak, Jr., "Native oxide top- and bottom-confined narrow stripe $p$-$n$ $Al_yGa_{1-y}As$-GaAs-$In_xGa_{1-x}As$ quantum well heterostructure laser," *Appl. Phys. Lett.*, vol. 63, pp. 1660–1662, 1993.
[89] K. D. Choquette, R. P. Schneider, Jr., K. L. Lear, and K. M. Geib, "Low threshold voltage vertical-cavity lasers fabricated by selective oxidation," *Electron. Lett.*, vol. 30, pp. 2043–2044, 1994.
[90] K. D. Choquette, K. L. Lear, R. P. Schneider, Jr., K. M. Geib, J. J. Figiel, and R. Hull, "Fabrication and performance of selectively oxidized vertical-cavity lasers," *IEEE Photon. Technol. Lett.*, vol. 7, pp. 1237–1239, 1995.
[91] H. Q. Hou, H. C. Chui, K. D. Choquette, B. E. Hammons, W. G. Breiland, and K. M. Geib, "Highly uniform and reproducible vertical-cavity surface-emitting lasers grown by metalorganic vapor phase epitaxy and *in situ* reflectometry," *IEEE Photon. Technol. Lett.*, vol. 8, pp. 1285–1287, 1996.
[92] K. D. Choquette, K. M. Geib, H. C. Chui, B. E. Hammons, H. Q. Hou, and T. J. Drummond, "Selective oxidation of buried AlGaAs versus AlAs layers," *Appl. Phys. Lett.*, vol. 69, pp. 1385–1387, 1996.
[93] M. H. MacDougal, G. M. Yang, A. E. Bond, C.-K. Lin, D. Tishinin, and P. D. Dapkus, "Electrically-pumped vertical-cavity lasers with $Al_xO_y$-GaAs reflectors," *IEEE Photon. Technol. Lett.*, vol. 8, pp. 310–312, 1996.
[94] D. L. Huffaker, J. Shin, and D. G. Deppe, "Lasing characteristics of low threshold microcavity lasers using half-wave spacer layers and lateral index confinement," *Appl. Phys. Lett.*, vol. 66, pp. 1723–1725, 1995.
[95] K. L. Lear, K. D. Choquette, R. P. Schneider, Jr., and S. P. Kilcoyne, "Modal analysis of a small surface emitting laser with selectively oxidized waveguide," *Appl. Phys. Lett.*, vol. 66, pp. 2616–2618, 1995.
[96] G. R. Hadley, "Effective index model for vertical-cavity surface-emitting lasers," *Opt. Lett.*, vol. 20, pp. 1483–1485, 1995.
[97] K. D. Choquette, K. L. Lear, R. P. Schneider, Jr., and K. M. Geib, "Cavity characteristics of selectively oxidized vertical-cavity lasers," *Appl. Phys. Lett.*, vol. 66, pp. 3413–3415, 1995.
[98] K. L. Lear, A. Mar, K. D. Choquette, S. P. Kilcoyne, R. P. Schneider, Jr., and K. M. Geib, "High-frequency modulation of oxide-confined vertical cavity surface emitting lasers," *Electron. Lett.*, vol. 32, pp. 457–458, 1996.
[99] R. F. Carson, M. L. Lovejoy, K. L. Lear, M. E. Warren, P. K. Seigal, D. C. Craft, S. P. Kilcoyne, G. A. Patrizi, and O. Blum, "Low-power approaches for parallel, free-space photonic interconnects," in *Proc. SPIE*, 1996, vol. CR62, pp. 35–63.
[100] D. Botez, L. Mawst, P. Hayashida, G. Peterson, and T. Roth, "High-pwer diode-laser arrays of closely-spaced "leaky" waveguides (antiguides)," *Appl. Phys. Lett.*, vol. 53, pp. 464–466, 1988.
[101] G. R. Hadley, K. D. Choquette, and K. L. Lear, "Understanding waveguiding in vertical-cavity surface emitting lasers," in *Proc. Integrat. Photon. Research Top. Meet.*, Boston, MA, Apr. 29–May 2, 1996, paper ITUE6.
[102] M. E. Warren, T. C. Du, J. R. Wendt, G. A. Vawter, R. F. Carson, K. L. Lear, S. P. Kilcoyne, R. P. Schneider, and J. C. Zolper, "Integration of diffractive lenses with addressable vertical-cavity laser arrays," in *Proc. SPIE*, 1995, vol. 2398, pp. 12–20.

**Weng W. Chow** received the Ph.D. degree in quantum optics.

He was Associate Professor of Physics and Astronomy at the University of New Mexico, Albuquerque, before joining Sandia National Laboratories, Albuquerque, NM. As a Senior Member of Technical Staff at Sandia, he is working on the application of microscopic theory to semiconductor laser device development. Some of this work is described in a book, *Semiconductor-Laser Physics*, which he co-authored. His other interests include laser gyros, phased arrays, coupled lasers, ignition of pyrotechnics with semiconductor lasers, and interferometric testing and analyses. He is an Adjoint Professor at the University of Arizona, Tucson.

Dr. Chow is a fellow of the Optical Society of America.

**Kent D. Choquette** (M'97) received B.S. degrees in engineering physics and applied mathematics from the University of Colorado, Boulder, in 1984 and the M.S. and Ph.D. degrees in materials science from the Universityof Wisconsin in 1985 and 1990, respectively.

After a post-doctoral appointment at AT&T Bell Laboratories, Murray Hill, NJ, in 1992 he joined Sandia National Laboratories, Albuquerque, NM. As a Senior Member of Technical Staff at Sandia, he has been engaged in research into novel fabrication and the physics of vertical-cavity surface-emitting lasers and other optoelectronic devices. He has written over 90 technical publications and 2 book chapters.

Dr. Choquette is a member of the Optical Society of America.

**Mary H. Crawford** received the B.A. degree in physics from Holy Cross College, Worcester, MA, in 1985 and the M.S. and Ph.D. degrees in physics from Brown University, Providence, RI, in 1987 and 1993, respectively. Her dissertation research involved gain spectroscopy and device physics of II–VI semiconductor light-emitting devices.

She joined Sandia National Laboratories, Albuquerque, NM, in 1993, where she is presently a Senior Member of Technical Staff. Her current research interests include optical characterization of wide bandgap compound semiconductor materials and heterostructure design and analysis of semiconductor light-emitting devices.

**Kevin L. Lear** (S'88–M'90) received the B.S.E.E. degree from the University of colorado, Boulder, in 1984, the M.S.E.E. degree in 1985, and the Ph.D.E.E. degree from Stanford University, Stanford, CA, in 1990. His thesis research involved resonant tunneling device structures and circuits.

In 1990, he joined Sandia National Laboratories as a Senior Member of Technical Staff. At Sandia, his principal concentration was on enhancing the performance and exploring the physics of vertical-cavity surface-emitting lasers (VCSEL's) including work on improving epitaxial mirrors, designing for high efficiency and high speed, and developing new structures. He also participated in the development of optoelectronic applications, heterojunction bipolar transistors, and research on quantum effect devices. In 1997, he became the Chief Scientific Officer at Micro Optical Devices, Inc., Albuquerque, NM, a small business commercializing VCSEL's.

Dr. Lear received the 1996 IEEE LEOS Distinguished Lecturer Award for his work at Sandia.

**G. Ronald Hadley** (SM'93) was born on November 25, 1946, in Memphis, TN. He received the B.A. degree in physics from Wichita State University, Wichita, KS, in 1968 and the Ph.D. degree in physics from Iowa State University in 1972.

Since receiving the Ph.D. degree, he has been employed at Sandia National Laboratories, Albuquerque, NM, where he has pursued a wide variety of research interests. He has authored or co-authored over 60 publications, most involving computer simulations of diverse phenomena including current flow in high-voltage vacuum diodes, two-phase flow of liquids through porous media, and the operation of solid-state and gas lasers. Since 1985, his research has centered in the area of photonics, and two-thirds of his publications have dealt with the numerical modeling of diode lasers or diffractive waveguide optics components. His most important recent contributions include new higher order accurate finite-difference algorithms for beam propagation, waveguide eigenmode computation, the modeling of reflective optical structures, and the simulation of vertical-cavity surface-emitting lasers.

Dr. Hadley is a member of the Optical Society of America.